Kent Academic Repository

Flame temperature reconstruction through multi-plenoptic camera technique

Flame temperature reconstruction through multi-plenoptic camera technique

Qi Qi[1], Md. Moinul Hossain[2], Biao Zhang[1], Tianxiang Ling[1], Chuanlong Xu[1]

[1] Key Laboratory of Energy Thermal Conversion and Control of Ministry of Education, School of Energy and Environment, Southeast University, 210096, Nanjing, China
[2] School of Engineering and Digital Arts, University of Kent, Canterbury, Kent, CT2 7NT, UK

E-mail: chuanlongxu@seu.edu.cn

Abstract

Due to the variety of burner structure and fuel mixing, the flame temperature distribution is not only irregular but also complex. Therefore, it is necessary to develop an advanced temperature measurement technique, which can provide not only adequate flame radiative information but also reconstruct complex flame temperature accurately. In this paper, a novel multi-plenoptic camera imaging technique is proposed which is not only provide adequate flame radiative information from two different directions but also reconstruct the complex flame temperature distribution accurately. An inverse algorithm i.e., Non-Negative Least Squares is used to reconstruct the flame temperature. The bimodal asymmetric temperature distribution is considered to verify the feasibility of the proposed system. Numerical simulations and experiments were carried out to evaluate the performance of the proposed technique. Simulation results demonstrate that the proposed system is able to provide higher reconstruction accuracy although the reconstruction accuracy decreases with the increase of noise levels. Meanwhile, compared with the single plenoptic and conventional multi-camera techniques, the proposed method has the advantages of lower relative error and better reconstruction quality even with higher noise levels. The proposed technique is further verified by experimental studies. The experimental results also demonstrate that the proposed technique is effective and feasible for the reconstruction of flame temperature. Therefore, the proposed multi-plenoptic camera imaging technique is capable of reconstructing the complex flame temperature fields more precisely.

1. Introduction

Combustion is widely applied in industrial processes such as power plants, aerospace engineering, solid propellant rockets, and ferrous metallurgy. Accurate measurement of flame temperature is significantly important to adjust the combustion mode, optimize the combustion process and control the pollutant emissions (NOx and CO). Due to the variety of burner structures and fuel mixing, the characteristics of the flame become complex. Therefore, it is desirable to develop an advanced measurement technique that can provide not only adequate flame radiative information but also reconstruct the complex flame temperature accurately. Over the past years, various measurement techniques were developed to obtain flame temperature [1]. They are mainly categorized into intrusive and non-intrusive techniques. For instance, the thermocouple is a typical intrusive, simple and intuitive temperature measurement technique and it measures

the flame temperature point-by-point. In addition, it affects the original structure of the flame thus the temperature distribution and combustion process [2, 3]. Therefore, this technique is restricted in many industrial processes. In contrast, the non-intrusive measurement techniques do not directly contact with the flame and thus no interference with the temperature distribution and the combustion process.

Various non-intrusive measurement techniques were reported based on acoustic computed tomography (CT), laser-based and radiative imaging [4-7]. For example, Zhang *et al* [8] used an acoustic CT to monitor the cross-sectional temperature of a boiler furnace and the temperature was reconstructed through an iterative algebraic reconstruction technique (ART). Yang *et al* [9] utilized a multiplexed tunable diode laser absorption spectroscopy (TDLAS) technique to obtain spatially resolved temperature information from a low-pressure premixed flame reactor. Although the acoustic CT techniques have been attracted extensive attention to the scientists, difficult to reconstruct three-dimensional (3-D) temperature distribution accurately due to poor resistance and high temperature of the furnace. Besides, due to the complexity of the optical path and higher cost of the system, the laser-based techniques are generally not suitable for abominably industrial environments. Among those techniques, the imaging-based radiative techniques have been recognized as effective and accurate for the flame temperature measurement. In addition, they are relatively simple in system setup, cost-effective and easy to manipulate for industrial environments. Based on sensing devices and computational techniques, they are divided into single-camera and multi-camera imaging techniques. For instance, Brisely *et al* [10] proposed a single-camera technique to reconstruct the cross-sectional temperature of a gas flame. Lu *et al* [11] also utilized a single-camera technique to measure the 3-D temperature of a flame. The single-camera techniques are simple but unable to reconstruct complex and turbulent flames temperature. Only suitable for stable or rotational symmetrical flames. The multi-camera techniques utilize multiple sensing devices (i.e., CCD/CMOS or optical imaging fiber) to obtain multiple perspective projections from different directions of a flame and to reconstruct the flame temperature. For example, Hossain *et al* [12, 13] proposed a multi-camera technique based on optical fiber sensing integrating CT and two-color pyrometry to reconstruct grey-level intensity and temperature of the flame. Zhou *et al* [1] developed a system with eight image detectors to capture monochromatic radiation intensity of a pulverized-coal-fired flame. Cheng *et al* [14] utilized four CCD detectors to reconstruct the 3-D temperature distribution of a gas-fired pilot tubular furnace flame. Floyd *et al* [15] used five cameras and number of mirrors located uniformly around the burner to obtain 48 projections of the flame. Although the multi-camera techniques are able to acquire more radiative information for reconstructing flame temperature, they are complex in setup, high cost due to the increase of multiple sensing devices. Also, a high degree of coupling and synchronization are required for the multi-camera techniques.

In recent years, single plenoptic camera (light field) technique has been attracted significant attention [16] in the area of combustion monitoring due to its capability of acquiring directions and positions information of the flame simultaneously in a single exposure. For instance, Sun *et al* [17, 18] applied a single light field camera to record 3-D radiative information of ethylene diffusion flame and a Least Square QR-factorization algorithm (LSQR) was used to reconstruct the flame temperature. Zhao *et al* [19] proposed an optical sectioning tomography with light field imaging techniques to measure the 3-D flame temperature. Huang *et al* [20] used a single plenoptic camera with Landweber method to reconstruct the 3-D temperature distribution. Li *et al* [21, 22] used various algorithms to analyze the flame radiative properties and temperature through light field image processing. Niu *et al* [23] utilized the light field image of ethylene flame to reconstruct 3-D temperature distribution, absorption and scattering coefficients to validate the reconstruction algorithm through numerical simulation. Yuan *et al* [24] utilized Monte Carlo method to analyze various participating media using the light-field camera imaging techniques. Although the single plenoptic camera is able to record directions and positions information of the flame simultaneously. However, the directional difference of the radiative information recorded by the single plenoptic camera is limited and thus rendering similar radiative information of the flame for the 3-D temperature reconstruction (such the plenoptic camera, R29 of Raytrix, the angle of the ray detected by the pixel is less than 0.015 °). The ill-conditioning and mathematical ambiguity will also worsen to solve the radiative information accurately. Result in, lower accuracy and resolution especially for complex and irregular turbulent flames. For the accurate 3-D flame temperature measurement, it is important to achieve sufficient radiative information with a larger directional difference and higher resolution. Where the multi-plenoptic camera can be used to achieve sufficient radiative information also to increase angular diversity. Meanwhile, Zhang *et al* [25] used two orthogonal-arranged focused light field cameras to reconstruct the 2-D flame temperature. In the field of particle image velocimetry (PIV), Fahringer *et al* [26] studied the plenoptic PIV with multiple plenoptic cameras.

This study presents a novel method to reconstruct the 3-D temperature of a flame based on multi-plenoptic camera (two plenoptic cameras in this study). The additional plenoptic camera increases the experimental complexity of the overall system. However, the complexity is marginal compared to other multi-camera techniques such as 8 detectors or five cameras and a number of mirrors. Moreover, the additional plenoptic cameras provide robustness and increase the

accuracy of the reconstruction technique [26]. A plenoptic imaging model is developed to acquire the flame radiative information from the multi-plenoptic camera and a Non-Negative Least Squares (NNLS) algorithm is used to reconstruct the flame temperature. Numerical simulations are carried out to evaluate the feasibility and practicality of the technique. The simulations are performed under bimodal asymmetrical flame temperature distribution under different noise levels. The results also compared with the single plenoptic camera and conventional multi-camera techniques and discussed in details. Experimental studies are also carried out to reconstruct the bimodal flame temperature under different combustion operating conditions. The results obtained from the experiments are also presented and discussed.

2. Measurement principle

2.1 System description

Figure 1 shows a schematic diagram of the proposed multi-plenoptic camera system. The system consists of two plenoptic cameras and a computer with application software. Two plenoptic cameras are placed at two different angles (θ is the angle between the plenoptic camera and X-axis, 45 ° and - 45 °) one side of the flame to obtain flame radiative information. The two plenoptic cameras are synchronised and controlled by the computer.

It is crucial to change the plenoptic camera parameters for the accurate flame temperature measurement in terms of radiation sampling. Because the parameters of the commercial plenoptic camera such as focal length and diameter of the microlens are usually fixed and not adjustable and they are may not be suitable to achieve accurate radiation sampling of the flame. So, the cage type plenoptic camera is adopted in this study. Figure 2 shows an example of the structure of the cage type plenoptic camera. The plenoptic camera mainly comprises a main lens, a microlens array, relay lens and charge-coupled device (CCD) sensor (IMPERX) along with the series of adaptors for connection and attachment. All components are installed using cage plates and fixed by cage rods. The relay lens is used to extend the imaging distance between the microlens array and the CCD sensor. Two Nikon 50 *mm* f/1.8D lenses are used in the cage system and connected head-to-head. The apertures of both lenses are fixed on f/1.8 for the maximum luminous flux and they both focused for infinity to achieve an accurate relay imaging. Such a symmetrical optical structure can eliminate the aberration at a decent level. The microlens array is mounted in a high-precision zoom housing which is not only adjusted microlens array's moving distance accurately but also guarantee it doesn't rotate during the movement. The microlens array manufactured by RPC Photonics, Inc. and its fill factor is 100%. These microlens arrays have a square aperture and a spherical profile. Related design of the cage type plenoptic camera can be found in [27, 28]. Each component of the two plenoptic cameras is the same.
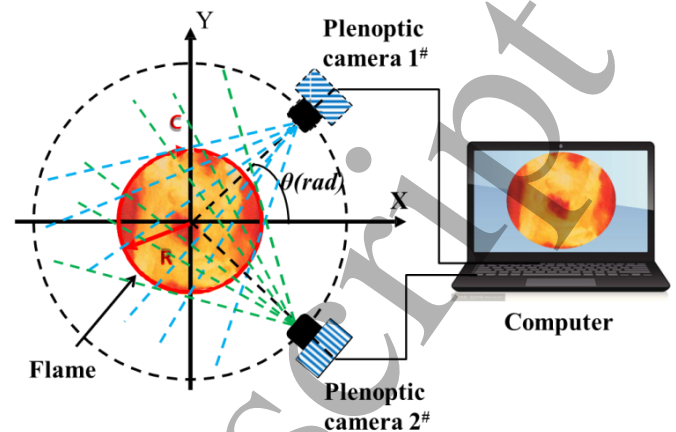
Figure 1. Schematic of the multi-plenoptic camera system
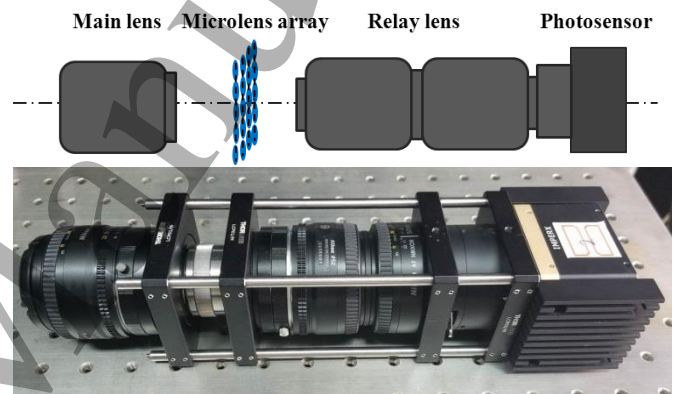
Figure 2. Example of the structure of the cage type plenoptic camera

2.2 Plenoptic imaging model

It is important to establish a plenoptic imaging model to acquire directional radiative information for a whole field of view (FOV). To achieve that a plenoptic imaging model is proposed in this study. Each of the cameras is treated as quasi-independently. Consequently, the single plenoptic imaging model is served as the basis for the multi-plenoptic camera technique. The plenoptic imaging model is divided into; 1) imaging by the main lens and 2) imaging by the microlens array. A pinhole camera model is used to trace the rays from pixel to the object [29]. It can be determined by the main lens plane and microlens array in the plenoptic camera. As shown in Figure 3, the pixel point 2 and virtual image point 1 is conjugated for the corresponding microlens and point 3 is their centre. Also, point 1 and virtual point 5 is conjugated for the main lens and point 0 is their center. Therefore, the coordinate (x_1, y_1, z_1) of point 1 can be derived from the following equations;

$$\frac{1}{L_{mp}} + \frac{1}{L_{mv}} = \frac{1}{f_m} \tag{1}$$

$$\frac{z_3 - z_2}{z_3 - z_1} = \frac{y_3 - y_2}{y_3 - y_1} = \frac{L_{mp}}{L_{mv}} \tag{2}$$

where (x_2, y_2, z_2) is the coordinate of point 2, (x_3, y_3, z_3) is the coordinate of point 3. L_{mv} is the distance between the virtual image plane and the microlens array. L_{mp} is the distance between the microlens array and photosensor. f_m and f are the focal length of the microlens and main lens, respectively. Similar way, the coordinate (x_5, y_5, z_5) of point 5 can be calculated by;

$$\frac{1}{L_{om}} + \frac{1}{L_{mv} + L_{mm}} = \frac{1}{f} \tag{3}$$

$$\frac{z_0 - z_1}{z_5 - z_0} = \frac{y_0 - y_1}{y_5 - y_0} = \frac{L_{mv} + L_{mm}}{L_{om}} \tag{4}$$

where (x_0, y_0, z_0) is the coordinate of point 0. L_{mm} is the distance between the main lens and the microlens array. L_{om} is the distance between the main lens and the centerline of flame. The direction of the flame radiation with the known coordinates of point 4 and 5 can be calculated by,

$$\theta_o = \arccos\left[\frac{(z_4 - z_5)}{\sqrt{L_{om}^2 + (y_4 - y_5)^2 + (z_4 - z_5)^2}}\right] \tag{5}$$

$$\psi_o = \begin{cases} \arctan\left(\dfrac{y_4 - y_5}{x_4 - x_5}\right), & y_4 \geq y_5 \\[3mm] \arctan\left(\dfrac{y_4 - y_5}{x_4 - x_5}\right) + 2\pi, & y_4 < y_5 \end{cases} \tag{6}$$

where θ_o and Ψ_o are the polar angle and azimuthal angle of the direction of the ray, respectively.
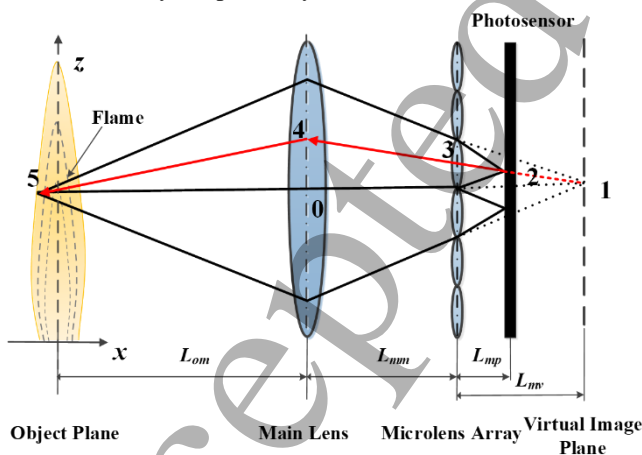
Figure 3. Schematic of flame radiation sampling with a plenoptic camera

2.3 A mathematical model for flame temperature

The intensity detected from a pixel is regarded as the intensity of the ray, which can be calculated using the Radiative Transfer Equation (RTE) [20].

$$\frac{d I_\lambda(s,\boldsymbol{s})}{d s} = -\kappa_{e\lambda}(s) I_\lambda(s,\boldsymbol{s}) + \kappa_{a\lambda}(s) I_{b\lambda}(s) + \frac{\kappa_{s\lambda}(s)}{4\pi} \int_{4\pi} I_\lambda(s,\boldsymbol{s}')\Phi(\boldsymbol{s}',\boldsymbol{s})d\Omega \tag{7}$$

where $I_\lambda(s,\boldsymbol{s})$ is the radiation intensity at position s and direction $\boldsymbol{s}$ at a wavelength of λ, $W/(m^3 \cdot sr)$; $I_{b\lambda}$ represents the blackbody radiative intensity at a wavelength of λ, $W/(m^3 \cdot sr)$; $\kappa_{e\lambda}(s)$, $\kappa_{a\lambda}(s)$, $\kappa_{s\lambda}(s)$ are the extinction, absorption, and scattering coefficients, respectively, (m^{-1}); $\Phi(\boldsymbol{s}', \boldsymbol{s})$ denotes the scattering phase function.

The extinction coefficient is the sum of the absorption and scattering coefficient. Because the soot particles are both absorptive and small (less than 0.1 μm) so the scattering contribution of the soot particles within flame is neglected. The Mie theory also verified that the scattering process of the participating media is assumed to be ignored and only the absorption is taken into consideration [30]. Hence, the Equation (7) can be simplified as follows;

$$\frac{d I_\lambda(s,\boldsymbol{s})}{d s} = -\kappa_{a\lambda}(s) I_\lambda(s,\boldsymbol{s}) + \kappa_{a\lambda}(s) I_{b\lambda}(s) \tag{8}$$

The radiation intensity of the flame $I_\lambda(s,\boldsymbol{s})$ along the detection path $(s,\boldsymbol{s})$ is then obtained by solving Equation (8) through the discretized solution as follows,

$$\begin{aligned} I_\lambda(s,\boldsymbol{s}) = &I_{b\lambda}^n \left[1 - \exp(-r_n \kappa_{a\lambda n}(r))\right] \\ &+ \sum_{i=1}^{n-1}\left[\exp\left(-\sum_{j=i+1}^n r_j \kappa_{a\lambda j}(r)\right) - \exp\left(-\sum_{j=i}^n r_j \kappa_{a\lambda j}(r)\right)\right] I_{b\lambda}^i \end{aligned} \tag{9}$$

where n is the total number of voxels that the flame radiation passes through, and each voxel is kept at a nearly uniform temperature. i and j are the ith and j^{th} voxel along the flame detection path $(s,\boldsymbol{s})$, respectively. r denotes the length of the detection path in the ith voxel. Hence, the out-going radiative intensity of the whole field can be obtained by integrating Equation (9) in different detection directions,

$$\begin{cases} I_{n\lambda 1}(s) = I_{b\lambda}^{n_1}\left[1-\exp(-r_{n_1}\kappa_{a\lambda n_1}(r))\right] + \sum_{i=1}^{n_1-1}\left[\exp\left(-\sum_{j=i+1}^{n_1}r_j\kappa_{a\lambda j}(r)\right) - \exp\left(-\sum_{j=i}^{n_1}r_j\kappa_{a\lambda j}(r)\right)\right]I_{b\lambda}^i \\[2mm] I_{n\lambda 2}(s) = I_{b\lambda}^{n_2}\left[1-\exp(-r_{n_2}\kappa_{a\lambda n_2}(r))\right] + \sum_{i=1}^{n_2-1}\left[\exp\left(-\sum_{j=i+1}^{n_2}r_j\kappa_{a\lambda j}(r)\right) - \exp\left(-\sum_{j=i}^{n_2}r_j\kappa_{a\lambda j}(r)\right)\right]I_{b\lambda}^i \qquad (10) \\[2mm] \vdots \\[2mm] I_{n\lambda M}(s) = I_{b\lambda}^{n_M}\left[1-\exp(-r_{n_M}\kappa_{a\lambda n_M}(r))\right] + \sum_{i=1}^{n_M-1}\left[\exp\left(-\sum_{j=i+1}^{n_M}r_j\kappa_{a\lambda j}(r)\right) - \exp\left(-\sum_{j=i}^{n_M}r_j\kappa_{a\lambda j}(r)\right)\right]I_{b\lambda}^i \end{cases}$$

It can be written as a linear equation and describe as follows:

$$\boldsymbol{I}_{n\lambda} = \boldsymbol{A}_\lambda \cdot \boldsymbol{I}_{b\lambda} \qquad (11)$$

where $\boldsymbol{I}_{n\lambda}$ is the flame radiative intensity vectors; $\boldsymbol{I}_{b\lambda}$ is the blackbody radiative intensity vectors. $\boldsymbol{A}_\lambda$ is the coefficient matrix. The dependence of blackbody radiative intensity $\boldsymbol{I}_{b\lambda}$ and the temperature T is expressed by,

$$I_{b\lambda}(r) = \frac{c_1\lambda^{-5}}{\pi\left[e^{c_2/\lambda T(r)}-1\right]} \qquad (12)$$

where c_1 is the first radiation constant, 3.7418×10^{-16} W·m², c_2 is the second radiation constant, 1.4388×10^{-2} m·K.

2.4 Inverse algorithm

It is required to solve the Equation (11) for the flame temperature reconstruction. In the inverse problem, the radiative intensities received by the photosensor $\boldsymbol{I}_\lambda$ regarded as input, the temperature field can be obtained based on the blackbody radiative intensity $\boldsymbol{I}_{b\lambda}$ and Equation (12). The equation (11) can be enormous due to the larger pixels covered by the flame image. Meanwhile, the number of the voxel that each ray crosses through is far less than the total number of the voxel, resulting in a sparse large and ill-conditioned matrix A with a large number of zeros. In this study, the Non-Negative Least Squares (NNLS) algorithm is used to solve Equation (11) and to receive the monochromatic intensity of blackbody radiation $I_{b\lambda}$ of each voxel. In this method, any negative intensity of calculated blackbody radiation is set zero and iterations are continued until converge. It ensures the non-negativity of the result and provides good stability. The detailed procedures of the NNLS algorithm can be found in Ref. [31].

$$Minimize\left\|A_\lambda\cdot I_{b\lambda}-I_{n\lambda}\right\| \text{ subject to } I_{b\lambda}\geq0 \qquad (13)$$

3. Simulation results and discussion

To evaluate the performance of the proposed system, numerical simulations are carried out to reconstruct the flame temperature. The bimodal asymmetric temperature distribution is used in this study and the detailed described in Section 3.1. The simulated flame is considered as a cylinder and the temperature range is set to $1000 – 2000$ K. Based on the experiment in Section 4, the radius (R) and axial length (Z)

of the simulated flame are 0.0066 m and 0.025 m, respectively. Based on the comparison results of the spatial resolution, the cylindrical flame is divided into 432 grids, that is circumferential (N_φ)×radial (N_r)×axial (N_z)= $12\times6\times6$. The absorption coefficient of ethylene flames is 0-30 m⁻¹ considered based on the Ref. [32, 33]. So, 10 m^{-1} is used in this study. The direction of the two plenoptic cameras are considered at -45° and 45° angles [34]. The simulations are also carried out for the single plenoptic camera with the directions of 45° and -45° angle. Similar angles are also considered for the conventional multi-camera systems to obtain the flame radiative information. The focal length of the main lens of the conventional camera is 50 mm, the distance between flame centerline to the main lens is 505 mm, the distance between the main lens and the photosensor is 55.5 mm. Their results are compared with the proposed system. The parameters of the plenoptic camera are shown in Table 1.

Table 1. Key parameters of the plenoptic camera

L_{om}	L_{mm}	L_{mp}	f	f_m	N_m	N_p	d_p	d_m
mm	mm	μm	mm	μm			μm	μm
505	53.1	480	50	600	60	12	8	95

N_m is the number of microlens along the horizontal/vertical direction of the microlens array. N_p is the number of pixels covered by each microlens array along the horizontal/vertical direction. d_p is the length of the pixels and d_m is the diameter of each microlens.

3.1 Bimodal asymmetric temperature distribution

In practical, the flame temperature distribution is complex and asymmetric. Therefore, it is required to examine the practicality and performance of the proposed technique under asymmetric and complex temperature distribution. To achieve that a bimodal asymmetric temperature distribution which has two-peak flame temperature is considered. It can be defined as follows [23];

Journal **XX** (XXXX) XXXXXX

Author *et al*

$$T(x,y,z) = \frac{2200}{3} \left\{ \begin{array}{l} \exp\left\{ \begin{array}{l} -40\left[(750x+7.5)/9-1.1\right]^2 \\ -25\left[(750y+8.5)/9-0.8\right]^2 \end{array} \right\} \\ +0.8\exp\left\{ \begin{array}{l} -25\left[(750x+7.5)/9-0.8\right]^2 \\ -35\left[(750y+8.5)/9-1.2\right]^2 \end{array} \right\} \end{array} \right\} \quad (14)$$

$$+880(1-100z/3)+753[\text{K}]$$

where x, y and z are the coordinates of the coordinate system, respectively. The bimodal asymmetric temperature distribution derived from the Equation (14) is shown in Fig. 4.

(a) Cross-sections   (b) Longitude-section at X = 0 *mm*
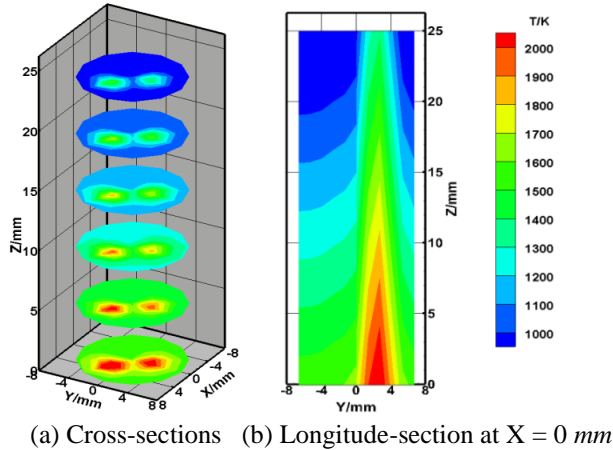
Figure 4. The temperature distribution of a bimodal asymmetric flame

3.2 Effects of Noise and Error Calculation

In order to investigate the performance of the proposed system, different noise levels are considered in this study. The noise levels are added randomly to the flame radiative intensity using Equation (15)[35]:

$$I_{mea} = (1+\sigma\zeta)I_{exa} \quad (15)$$

where I_{mea} is the measured radiative intensity exiting boundaries, ζ is a standard normal distribution random variable with zero mean and standard unit deviation. The standard deviations of measured transmittance and reflectance σ and for a γ measured error at 99% confidence are determined as

$$\sigma = \frac{I_{exa} \times \gamma}{2.576} \quad (16)$$

In this study, the $\gamma = 1\%$, 3% and 5% are considered. To evaluate the performance, the relative error of the reconstructed temperature ΔT and mean relative error ΔT_{mean} are calculated and defined as follows;

$$\Delta T_i = \frac{\left| T_{rst,i} - T_{ori,i} \right|}{T_{ori,i}} \quad (17)$$

$$\Delta T_{mean} = \frac{1}{N} \sum_{i=1}^{n} \Delta T_i \quad (18)$$

where $T_{rst,i}$ is the reconstructed temperature, $T_{ori,i}$ is the original temperature, N is the total number of grids.
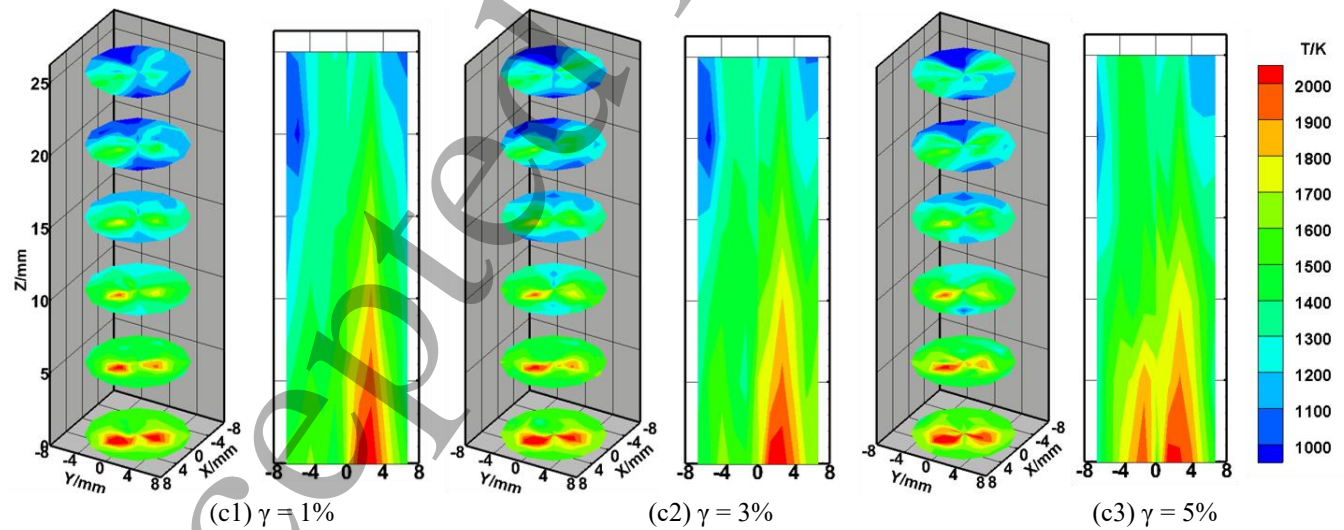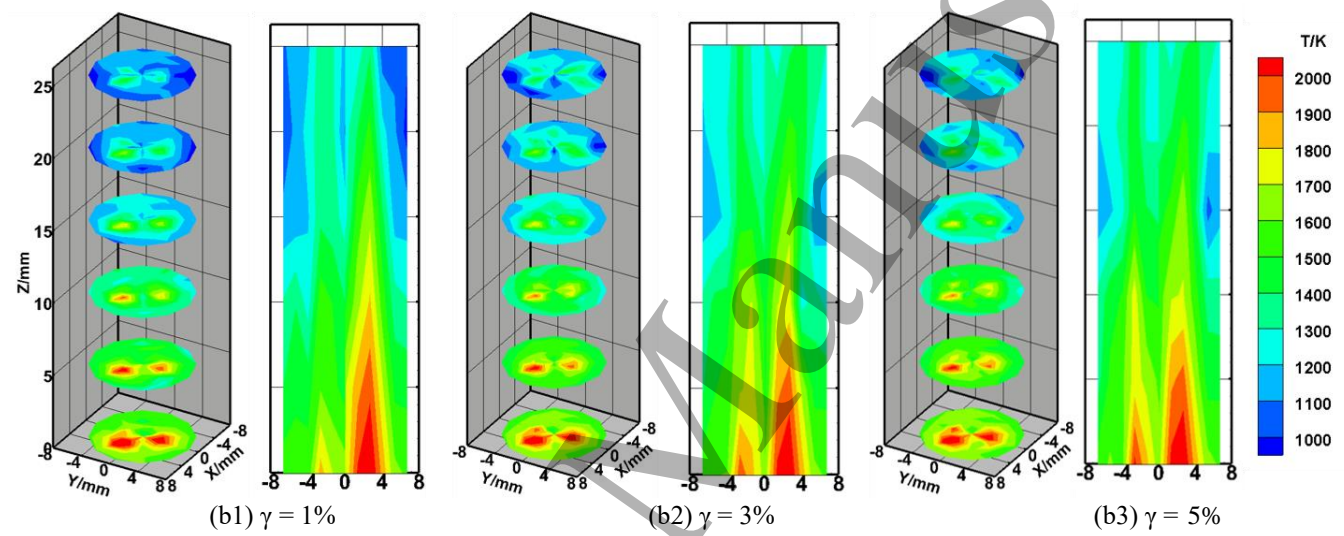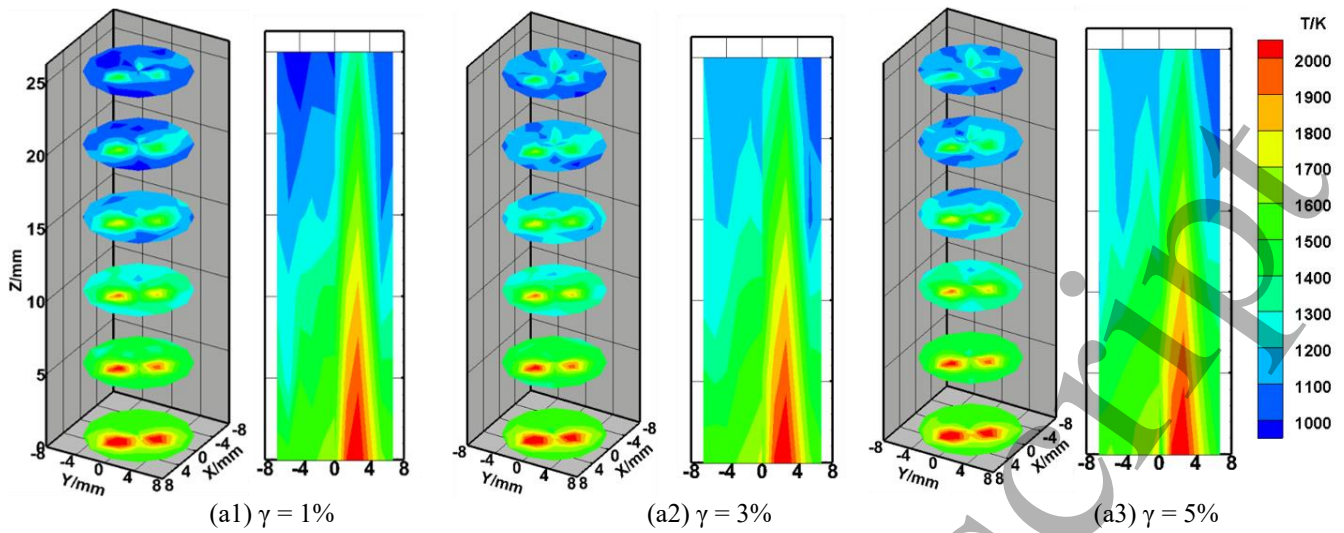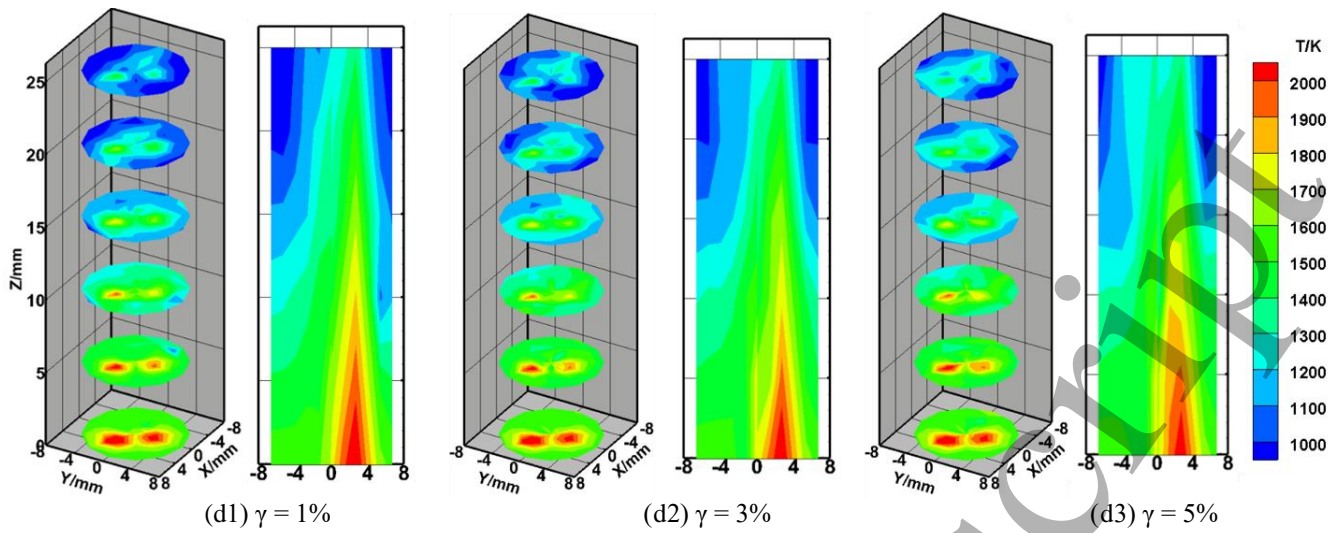
3.3 Numerical simulation results

Figure 5 shows the simulated flame images obtained from the plenoptic [Fig. 5(a)] and the conventional multi-camera [Fig. 5(b)] systems. It can be seen that the radiative intensity distribution is not continuous due to the microlens array in the plenoptic camera. On the contrary, the radiative distribution is continuous for the conventional camera. For the bimodal asymmetric condition, the distributions of the flame radiative intensity are non-uniform at angles -45 ° and 45 ° as shown in Figure 5. Where the simulated flame images manifest the complex temperature distribution at different angles.

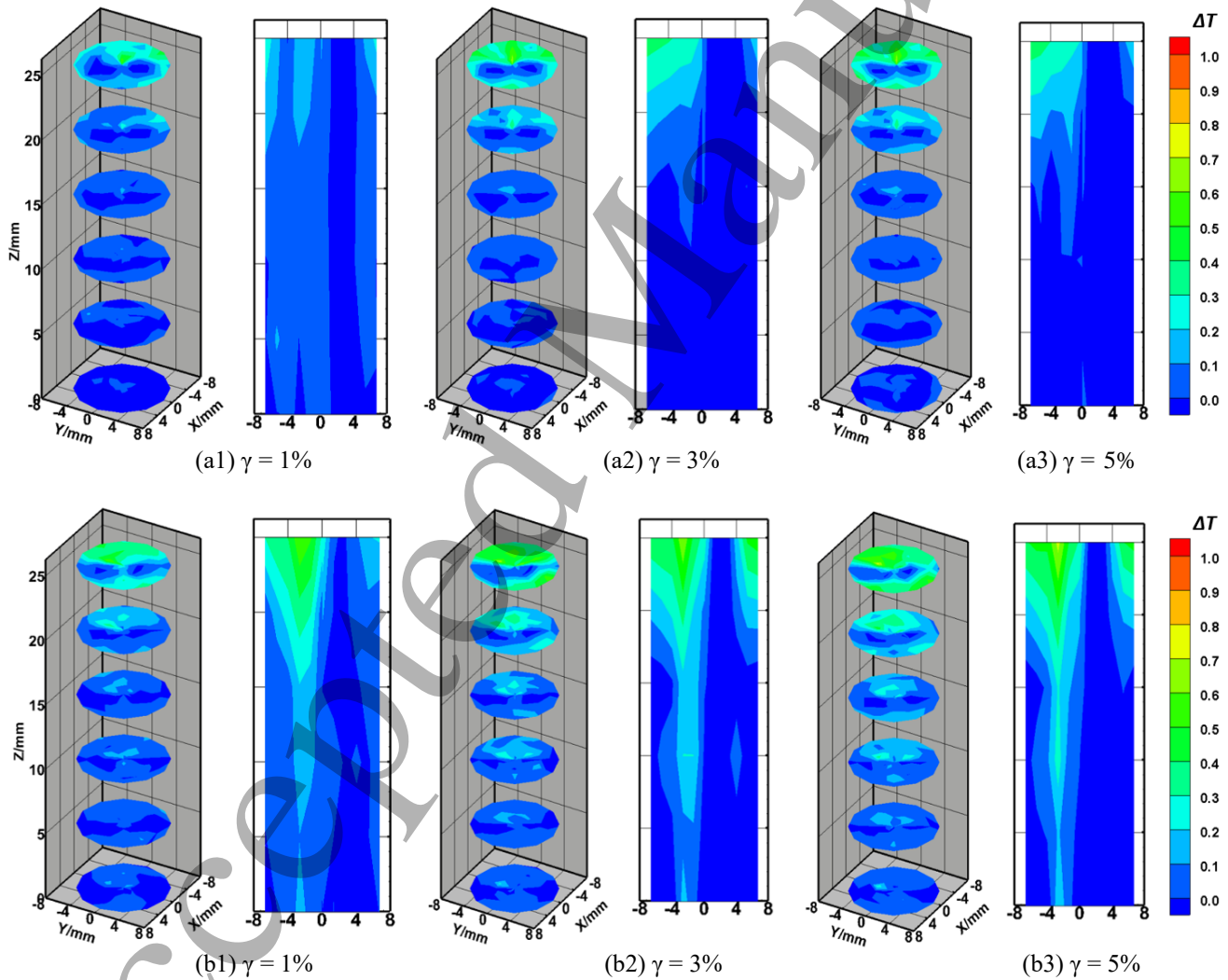(a) Plenoptic camera   (b) Conventional camera
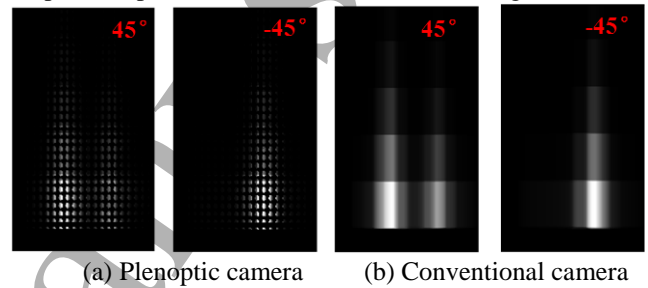
Figure 5. Simulated flame images at different angles under the bimodal asymmetric distribution

The reconstructed temperature and the relative error distributions of the simulated flame under different noise levels are shown in Figures 6 and 7. They are compared with the original temperature distribution [Fig. 4]. The reconstructed temperature distributions are almost similar to the original distribution for the multi-plenoptic camera system, although the results show small perturbations. For the proposed system, it has been observed that better reconstruction accuracy can be achieved even when the noise level is $\gamma = 5\%$. For the single plenoptic camera system, false and artefacts temperature distributions can be seen at the top and bottom parts of the reconstructed temperature distributions with the increase of γ. Compare to the single plenoptic camera system with the proposed system, it can be seen that both system exhibit the bimodal shape from the cross-sections. A bimodal structure appeared at the bottom of the flame from the longitude section at X = 0 *mm* when $\gamma = 5\%$. For the conventional multi-camera system, better reconstruction results are observed compared to the single plenoptic camera. but the reconstructed temperature distribution shows a larger perturbation particularly at the top part when $\gamma = 5\%$.

(a1) γ = 1%

(a2) γ = 3%

(a3) γ = 5%

(b1) γ = 1%

(b2) γ = 3%

(b3) γ = 5%

(c1) γ = 1%

(c2) γ = 3%

(c3) γ = 5%

(d1) γ = 1%   (d2) γ = 3%   (d3) γ = 5%

Figure 6. The reconstructed temperature distribution of the simulated flame；(a) Proposed system (b) Single camera system at angle 45 °(c) Single camera system at an angle -45 °and (d) Conventional multi-camera system

(a1) γ = 1%   (a2) γ = 3%   (a3) γ = 5%

(b1) γ = 1%   (b2) γ = 3%   (b3) γ = 5%

(c1) γ = 1%　　　　　　　　　　(c2) γ = 3%　　　　　　　　　　(c3) γ = 5%


(d1) γ = 1%　　　　　　　　　　(d2) γ = 3%　　　　　　　　　　(d3) γ = 5%
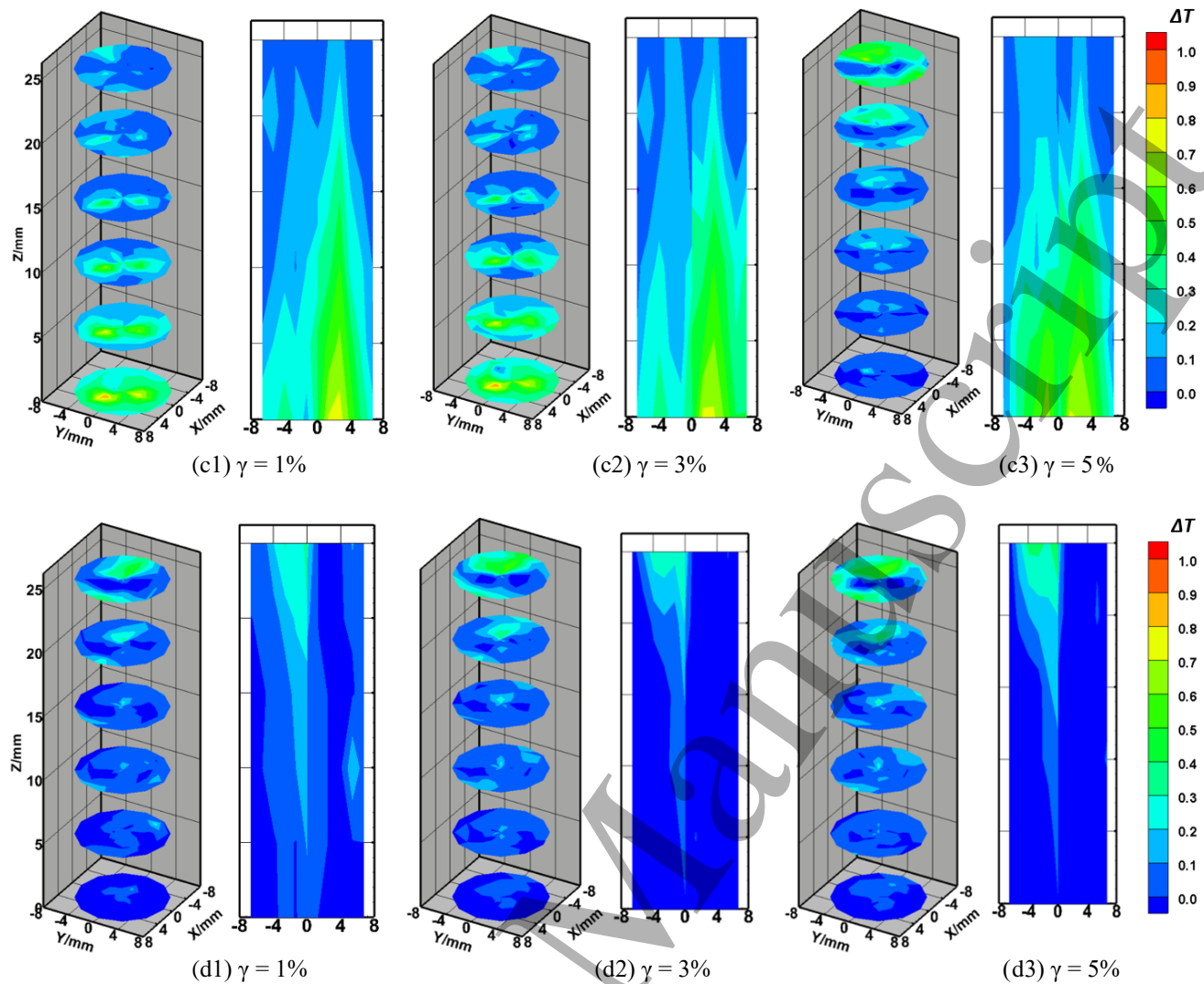
Figure 7. The reconstructed relative error distribution of simulated flame temperature；(a) Proposed system (b) Single camera system at angle 45 °(c) Single camera system at an angle -45 °and (d)Conventional multi-camera system

Figure 7 shows the distributions of reconstructed relative error of the bimodal asymmetric flame temperature under the three different noise levels. It can be seen that the better reconstruction quality is achieved for the proposed technique compared to the single and conventional multi-camera techniques, especially in the bottom regions of the temperature field. Moreover, the relative errors of the multi-plenoptic camera system exhibit much more accurate than the other three systems. In comparison to the 45 ° and the -45 °for the single plenoptic camera system, it can be seen that the 45 ℃case demonstrates a higher accuracy than -45 ° case. Because the bimodal shape of flame can be seen from the simulated image at an angle of 45 °. However, only one peak is captured in the simulated image at an angle -45 °. Thus, it is necessary to use a multi-plenoptic camera to obtain flame radiation information to reconstruct bimodal flame temperature accurately. Although the reconstructed regions with large perturbation

increase with the increase of the noise levels, the proposed system still demonstrated higher stability.

Author *et al*
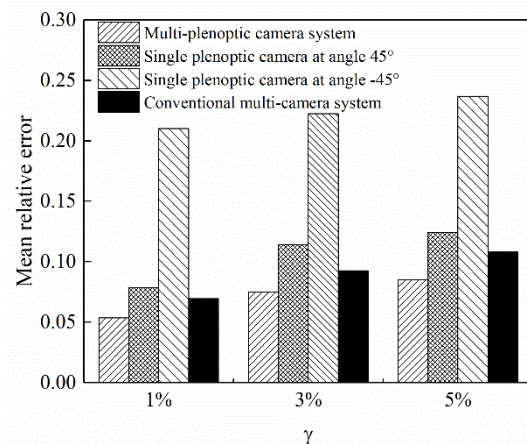
Figure 8. The mean relative error of temperature with different noise levels

Table 2. The number of grids ($\Delta T > 0.1$)

System	$\gamma = 1\%$	$\gamma = 3\%$	$\gamma = 5\%$
Proposed system	83	110	128
Single camera system at angle 45°	133	180	201
Single camera system at angle -45°	324	340	354
Conventional multi-camera system	116	149	168

The mean relative errors of the reconstructed bimodal asymmetric flame temperature are shown in Figure 8. The mean reconstruction error increases with the increase of noise level. For the proposed system, the mean reconstruction error are only 5.35%, 7.52%, and 8.49% for the $\gamma = 1\%$, $\gamma = 3\%$, $\gamma = 5\%$, respectively. When the $\gamma = 5\%$, the mean relative errors for the conventional multi-camera and single plenoptic camera system at the angle 45° are all above 10%. For the single plenoptic camera at angle -45°, the mean relative error even reaches 20%, which is not able to reconstruct the bimodal flame temperature perfectly. In addition, the flame is discretized into 432 grids, the number of grids with $\Delta T > 0.1$ is summarized in Table 2. It can be seen that the number of grids ($\Delta T > 0.1$) is increased with the added noise level. When the noise level $\gamma = 1\%$, the proportion between the number of grids ($\Delta T > 0.1$) and the total number of grids is less than 20% for the proposed system. However, for the other three systems, the proportion is more than 25% and even 72% for the single camera at angle -45° system. When the noise level γ reaches 5%, the proportion is higher. For the single camera system even reached 354 at angle -45°. Thereby, the results obtained from the simulations demonstrate that the bimodal asymmetric flame temperature can be reconstructed accurately by the multi-plenoptic camera technique even with the higher level of noises.

4. Experimental results and discussion

4.1 Experimental setup

To validate the proposed multi-plenoptic camera system, experiments are carried out to reconstruct ethylene bimodal flame temperature distribution. To avoid the influence of the stray radiation, the experiments were performed in a dark room. Figure 9 shows the experimental setup. It mainly consists of two parts, one is a co-flow burner, the other is the multi-plenoptic camera system. In order to generate a multi-peak flame, a rod of width 8 *mm* is placed at the exit of the burner which diameter is 10 *mm* [36]. The detailed descriptions of the burner structure and the parameters can be found elsewhere in Ref. [18]. Two plenoptic cameras are placed on the two parallel sliding rails, which are parallel to the burner to obtain the flame images from two directions. The lifting, rotating platform and the supporting plate are assembled together which is fixed on the sliding rail to sustain the camera. Therefore, the translation, rotation and lifting of the camera can be achieved. Two cameras were calibrated relative to each other by acquiring target images at their respective positions. The target was basically a cylinder 60 *mm* diameter by 10 *mm* height and positioned vertically at the center of the burner nozzle. Alignment between two cameras is determined by comparing the locations of the perpendicular and the centerline of the cylinder. The differences are found less than 5 pixels in the vertical and horizontal direction. Camera 1# is placed at the 45°, and camera 2# is placed at the -45°. The exposure time of the two cameras is set to 170 *μs*. The focal length of the main lens is 50 *mm*. The size of the microlens is 100×100 *μm* and $f\# = 4.2$, respectively. The CCD sensor of the plenoptic camera has a resolution of 3312 (H) $\times 2488$ (V), the pixel size is 5.5 *μm*. The corresponding wavelengths of the λ_R, λ_G and λ_B channel of the sensor are 610 *nm*, 530 *nm* and 460 *nm*, respectively.

4.2 Radiation intensity calibration

In order to obtain the relationship between the gray level and the radiation intensity, a blackbody furnace (LANDCAL R1500T) is used to calibrate the radiation intensity of the plenoptic CCD sensor. Based on the Equation (11), there is a one-to-one relationship between the temperature of the blackbody furnace and the radiation intensity detected by the CCD sensor. The temperature range of the blackbody furnace is 1173 *K* to 1523 *K*, the temperature interval is 50 *K*. Figure 10 shows the example of blackbody radiation images captured by the plenoptic camera under different temperature settings.

The radiation intensity of R (red) channel is more sensitive to grey level than those of G (green) and B (blue) channels. Therefore, only used the R channel to obtain the relationship between the gray level and corresponding radiation intensity. The exposure time of the plenoptic camera is set to 170 *μs*. Two plenoptic cameras are calibrated separately and the fitted results of the R channel is shown in Figure 11.

4.3 Experimental results

During the experiments, two combustion operating conditions are created to investigate the performance of the proposed system. The volumetric flow rates of fuel and air are supplied 90 *ml/mim* and 1 *m³/h* for case 1, 130 *ml/min* and 0.3 *m³/h* for case 2. Figure 12 shows the example of flame images captured by the proposed system from two different directions. It has been observed that the captured images are distinct depending on the direction of the camera. The flame images exhibit different shapes for different directions.
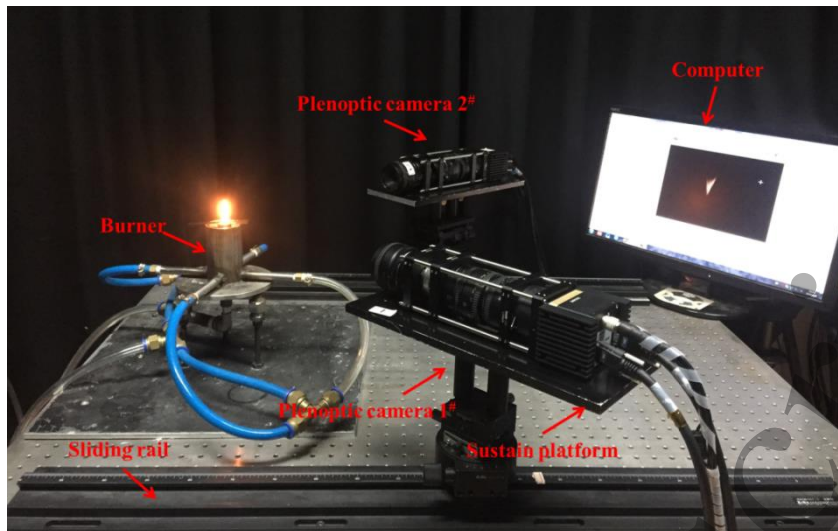
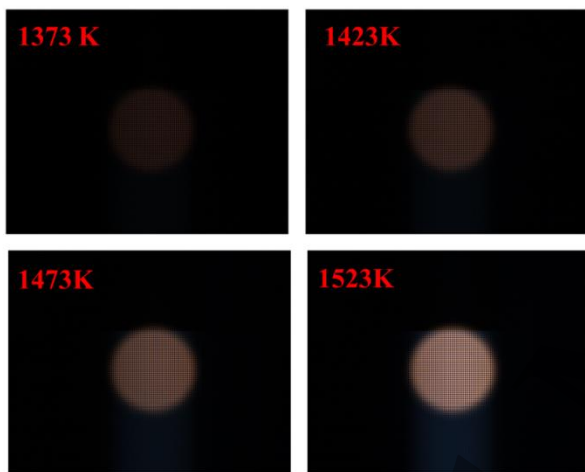**Figure 9.** The experimental setup of the multi-plenoptic camera system

Figure 10. Example of the blackbody furnace images under different temperature settings
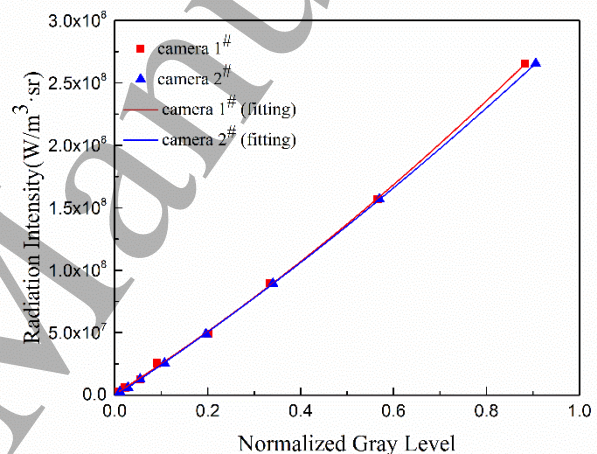

Figure 11. The relationship between the blackbody images and corresponding radiation intensity

The computational domain is treated as a cylinder and the flame temperature fields are divided into 6000 grids, that is $N_\varphi \times N_r \times N_z = 20 \times 20 \times 15$. In this study, the absorption coefficient value is set to 10 m^{-1} [33]. The NNLS algorithm is used to reconstruct the flame temperature. The noise of the CCD sensor was eliminated by subtracting gray levels of the dark image from the raw image. The dark image was captured when the camera is fully capped with no external light. Figure 13 shows the reconstruction temperature distributions over five longitude-sections along Y-axis of ethylene bimodal flame. It can be seen that the reconstructed temperature distributions are within the range of 800 K - 1700 K. The results have shown similar agreement with the results obtained by other researchers [17].

Figures 12 and 13 exhibits the similarities and differences of flame shape between captured images and reconstructed distributions. Firstly, Figures 13(a) and 13(b) exhibit the overall reconstructed flame shape as expected, such as the overall bimodal of the flame, the height of both peaks of the flame (the fact that the right peak is taller than the left one), and the distance between the two peaks. Secondly, Figures 13(a) and 13(b) also exhibit some differences of temperature distribution with more detailed level as expected.

It can also be observed from Figures 13(a) and 13(b) that along the Y-axis, the flame temperature distribution for each section is different. For each section, the flame temperature increases and then decreases from the outlet of the burner to the surroundings.

The variations of the two peaks have the largest influence on the flame temperature measurement, where the highest resolution is required [37]. To date, various studies used a single plenoptic camera for the reconstruction of flame temperature with the flame voxels of $N_\varphi \times N_r \times N_z = 4 \times 4 \times 6$ [18], $N_\varphi \times N_r \times N_z = 1 \times 7 \times 7$ [20] and $N_\varphi \times N_r \times N_z = 1 \times 6 \times 6$ [23], respectively. The spatial resolution of their studies is low. In this study, the spatial resolution is improved (i.e., $N_\varphi \times N_r \times N_z = 20 \times 20 \times 15$) with the aid of utilising two plenoptic cameras thus the reconstruction result has a higher resolution. Finally, the experimental results indicate that the multi-plenoptic camera system is feasible for reconstructing the complex flame temperature distribution more precisely.

(a) Case 1

(b) Case 2
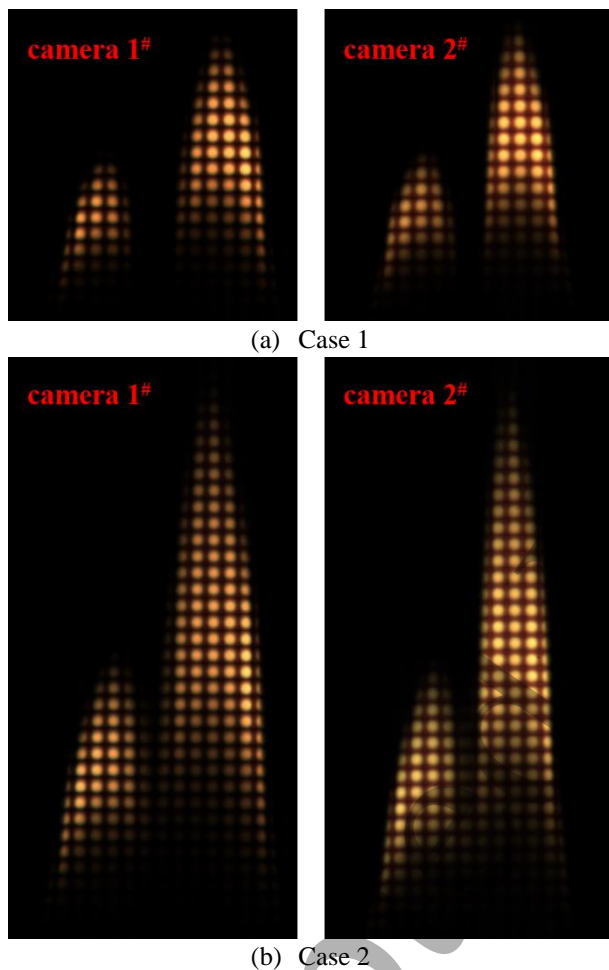
Figure 12. Example of ethylene flame images captured by the proposed system under different combustion conditions

(a) Case 1

(b) Case 2
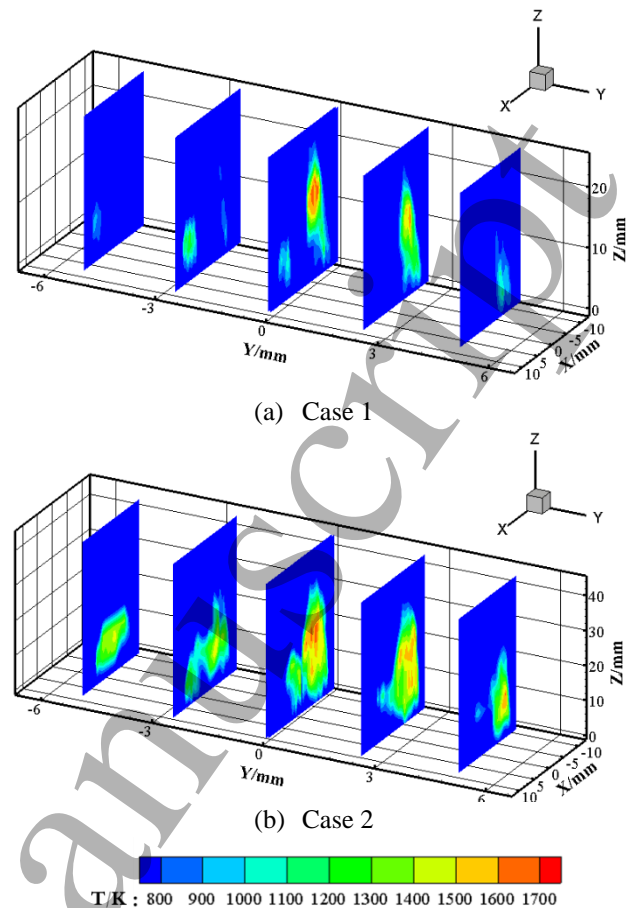
Figure 13. The reconstructed temperature distributions over five longitude-sections of ethylene bimodal flames

6. Conclusions

In this paper, a multi-plenoptic camera technique is proposed to reconstruct the flame temperature. Numerical simulations and preliminary experiments are carried out to validate the proposed technique. A plenoptic imaging model is developed to obtain the directional radiative intensity of the flame. The Non-Negative Least Square algorithm is used to reconstruct the simulated flame temperature. The simulation results show that the flame temperature can be reconstructed accurately by the proposed technique and the reconstruction accuracy remains higher even with the noise level of $\gamma = 5\%$. The mean relative error is calculated to evaluate the system. The mean relative error is smaller for the bimodal temperature distribution compared to the single plenoptic and the conventional multi-camera techniques. The experimental results indicate that the proposed technique is capable of reconstructing the 3-D flame temperature field with a higher spatial reconstruction resolution. Thus, the proposed technique has the potential to measure the complex and irregular flame temperature distribution.

Acknowledgements

References

[1] Zhou H-C, Lou C, Cheng Q, Jiang Z, He J, Huang B, Pei Z and Lu C 2005 Experimental investigations on visualization of three-dimensional temperature distributions in a large-scale pulverized-coal-fired boiler furnace *Proc. Combust. Inst.* **30** 1699-706

[2] Hindasageri V, Vedula R P and Prabhu S V 2013 Thermocouple error correction for measuring the flame temperature with determination of emissivity and heat transfer coefficient *Rev. Sci. Instrum.* **84** 82

[3] Yilmaz N, Gill W, Donaldson A B and Lucero R E 2008 Problems Encountered in Fluctuating Flame Temperature Measurements by Thermocouple *Sensors (Basel)* **8** 7882-93

[4] Denisov A, Colmegna G and Jansohn P 2014 Temperature measurements in sooting counterflow diffusion flames using laser-induced fluorescence of flame-produced nitric oxide *Appl. Phys. B* **116** 339-46

[5] Tolles W M, Nibler J W, Mcdonald J R and Harvey A B 1977 A Review of the Theory and Application of Coherent Anti-Stokes Raman Spectroscopy (CARS) *Appl. Spectrosc.* **31** 253-71

[6] Zhang X 2014 Simultaneous Measurement of Three-Dimensional Temperature Distributions and Radiative Properties Based on Radiation Image Processing Technology in a Gas-Fired Pilot Tubular Furnace *Heat Transfer Eng.* **35** 770-9

[7] Zheng L 2011 *Oxy-Fuel Combustion for Power Generation and Carbon Dioxide (Co2) Capture*

[8] Zhang S, Shen G, An L and Niu Y 2015 Online monitoring of the two-dimensional temperature field in a boiler furnace based on acoustic computed tomography *Appl. Therm. Eng.* **75** 958-66

[9] Yang H N, Yang B, Cai X S, Hecht C, Dreier T and Schulz C 2015 Three-Dimensional (3-D) Temperature Measurement in a Low Pressure Flame Reactor Using Multiplexed Tunable Diode Laser Absorption Spectroscopy (TDLAS) *Lasers in Eng.* **31** 285-97

[10] Brisley P M L G, Yan Y 2005 Three-dimensional temperature measurement of combustion flames using a single monochromatic CCD camera *IEEE Trans. Instrum. Meas.* **54** 1417-21

[11] Lu Y, S-M W and Z Z 1998 3-Dimensional Irradiance Imaging with a Single Camera System *Journal of Southeast University(English Edition)* 40-4

[12] Hossain M M, Lu G, Sun D and Yan Y 2012 Three-dimensional reconstruction of flame temperature and emissivity distribution using optical tomographic and two-colour pyrometric techniques *Meas. Sci. Technol.* **24** 55-

[13] Hossain M M M, Lu G and Yan Y 2012 Optical Fiber Imaging Based Tomographic Reconstruction of Burner Flames *IEEE Transactions on Instrumentation & Measurement* **61** 1417-25

[14] Cheng Q, Zhang X, Wang Z, Zhou H and Shao S 2013 Simultaneous Measurement of Three-Dimensional Temperature Distributions and Radiative Properties Based on Radiation Image Processing Technology in a Gas-Fired Pilot Tubular Furnace *Heat Transfer Eng.* **35** 770-9

[15] Floyd J and Kempf A M 2011 Computed Tomography of Chemiluminescence (CTC): High resolution and instantaneous 3-D measurements of a Matrix burner *Proc. Combust. Inst.* **33** 751-8

[16] Todor Georgiev A L 2010 Focused Plenoptic Camera and Rendering Focused Plenoptic Camera and Rendering *J. Electron. Imaging* **19** 021106

[17] Sun J, Hossain M M, Xu C and Zhang B 2018 Investigation of flame radiation sampling and temperature measurement through light field camera *Int. J. Heat Mass Transfer* **121** 1281-96

[18] Sun J, Xu C, Zhang B, Hossain M M, Wang S, Qi H and Tan H 2016 Three-dimensional temperature field measurement of flame using a single light field camera *Opt. Express* **24** 1118-32

[19] Zhao W , Zhang B and C X 2018 Optical Sectioning Tomographic Reconstruction of Three-dimensional Flame Temperature Distribution Using Single Light Field Camera *IEEE Sensors Journal* **18**:528-39

[20] Huang X, Qi H, Zhang X-L, Ren Y-T, Ruan L-M and Tan H-P 2018 Application of Landweber Method for Three-Dimensional Temperature Field Reconstruction Based on the Light-Field Imaging Technique *J. Heat Transfer* **140** 082701

[21] Li T Z C, Yuan Y Flame temperature estimation from light field image processing

[22] Li T-J, Li S-N, Yuan Y, Wang F-Q and Tan H-P 2018 Light field imaging analysis of flame radiative properties based on Monte Carlo method *Int. J. Heat Mass Transfer* **119** 303-11

[23] Niu C-Y, Qi H, Huang X, Ruan L-M and Tan H-P 2016 Efficient and robust method for simultaneous reconstruction of the temperature distribution and radiative properties in absorbing, emitting, and scattering media *J. Quant. Spectrosc. Radiat. Transfer* **184** 44-57

[24] Yuan Y, Liu B, Li S and Tan H-P 2016 Light-field-camera imaging simulation of participatory media using Monte Carlo method *Int. J. Heat Mass Transfer* **102** 518-27

[25] Zhang B, Wang S, Xu C and Wang S 2017 A fast inversion method for 2-D flame temperature measurement. In: *Instrumentation and Measurement Technology Conference,* pp 1-6

[26] Fahringer T W and Thurow B S 2018 Plenoptic particle image velocimetry with multiple plenoptic cameras *Meas. Sci. Technol.* **29** 075202

[27] Levoy M, Zhang Z and Mcdowall I 2010 Recording and controlling the 4D light field in a microscope using microlens arrays *J. Microsc.* **235** 144-62

[28] Zhang Z Examples of Light Field Micrographs (2007). http://graphics.stanford.edu/projects/lfmicroscope/2 007.html)

[29] Sun J, Hossain M M, Xu C-L, Zhang B and Wang S-M 2017 A novel calibration method of focused light field camera for 3-D reconstruction of flame temperature *Opt. Commun.* **390** 7-15

[30] Felske J D and Tien C L 1973 Calculation of the Emissivity of Luminous Flames *Combustion Science & Technology* **7** 25-31

[31] Lawson C L and Hanson R J 1995 *Solving least squares problems* vol 15 (Philadelphia: Siam)

[32] Santoro R J, Yeh T T, Horvath J J and Semerjian H G 1987 The Transport and Growth of Soot Particles in Laminar Diffusion Flames *Combustion Science & Technology* **53** 89-115

[33] Li T-J, Zhang C-X, Yuan Y, Shuai Y and Tan H-P 2019 Effect of nonuniform radiation properties on flame temperature reconstruction based on light field imaging *Int. Commun. Heat Mass Transfer* **104** 136-46

[34] Liu H, Wang Q and Cai W 2019 Assessment of plenoptic imaging for reconstruction of 3D discrete and continuous luminous fields *Journal of the Optical Society of America A* **36** 149-58

[35] Niu C-Y, Qi H, Huang X, Ruan L-M, Wang W and Tan H-P 2015 Simultaneous reconstruction of temperature distribution and radiative properties in participating media using a hybrid LSQR–PSO algorithm *Chin. Phys. B* **24** 114401

[36] Wu Y, Lei Q and Ma L 2014 Experimental demonstration of 4D imaging in two-phase flows based on computed tomography at 5 kHz *Appl. Opt.* **53** 5547

[37] Snelling D R, Thomson K A, Smallwood G J, -Oslash, G-uacute L, lder, Weckman E and Fraser R 2002 Spectrally resolved measurement of flame radiation to determine soot temperature and concentration *AIAA journal* **40** 1789-95